## PAPER

Check for updates

# Removal of anthracene in water by MIL-88(Fe), NH₂-MIL-88(Fe), and mixed-MIL-88(Fe) metal–organic frameworks†

Zakariyya Uba Zango,[a] Khairulazhar Jumbri,[a] Nonni Soraya Sambudi,[b] Noor Hana Hanif Abu Bakar,[c] Nor Ain Fathihah Abdullah,[a] Chanbasha Basheer[d] and Bahruddin Saad [ID] *[a]

Three adsorbents based on the metal–organic frameworks (MOFs), *viz.*; MIL-88(Fe), NH₂-MIL-88(Fe), and mixed-MIL-88(Fe) were synthesized using a microwave-assisted solvothermal technique. The as-synthesized MOFs were characterized by X-ray diffraction (XRD), Brunauer–Emmett–Teller (BET), field emission scanning microscopy (FESEM), X-ray photoelectron spectroscopy (XPS), thermogravimetric analysis (TGA), and Fourier transform infrared spectroscopy (FTIR). The MOFs were shown to possess highly crystalline and porous structures with specific surface areas of 1240, 941, and 1025 $m^2 g^{-1}$ and pore volumes of 0.7, 0.6 and 0.6 $m^3 g^{-1}$ for MIL-88(Fe), NH₂-MIL-88(Fe) and mixed-MIL-88(Fe), respectively. Faster removal of a model polycyclic aromatic hydrocarbon, anthracene (ANT) within 25 minutes, was achieved when these MOFs were used as adsorbents in water. The removal efficiency was 98.3, 92.4 and 95.8% for MIL-88(Fe), NH₂-MIL-88(Fe) and mixed-MIL-88(Fe), respectively. The kinetics and isotherms of the process were best statistically described by pseudo-second-order and Langmuir models, respectively, while the thermodynamic studies revealed the exothermic and spontaneous nature of the process. Docking simulations were found to be consistent with the experimental results with MIL-88(Fe) showing the best binding capacity with the ANT molecule.

## Introduction

The frequent detection of toxic contaminants such as polycyclic aromatic hydrocarbons (PAHs) in environmental samples such as surface water, soil, and foods has caused much public concern. PAHs are introduced into water from various anthropogenic sources such as petroleum products, mining of coal, coke production, incomplete combustion of carbonaceous materials, discharge of wastewater from petrochemical industries, leakage of engine oils, *etc.*[1] Thus, they are contributing to the persistent problem of pollution of the aquatic environment, which results in climate change and subsequent destruction of the ecosystem.[2,3] Release of PAHs has been more prominent in countries with high population and industries. China alone releases about 2300 tonnes of

PAHs which accounts for about 22% of total global emission.[4] Anthracene (ANT) (Fig. 1) is one of the most toxic PAHs that has been ubiquitously detected in various environmental samples, particularly surface water, sewage sludge, and foods. When present in water, it does not undergo photodegradation due to its high lipophilic nature.[5] It is highly resistant to biodegradation compared to other PAHs such as phenanthrene and pyrene,[6] and can easily enter the food chain through water.[7,8] PAHs have been linked to serious diseases such as cancer (particularly lung cancer), cardiovascular disorders, and defects in reproductive system, among others.[9] Thus, they are classified as endocrine disruptors and 16 of them have been listed as carcinogenic and mutagenic by the United States Environmental Protection Agency (USEPA).[10] Their widespread presence in water demands effective methods for their removal.

Various techniques for wastewater remediations such as coagulation, flocculation,[11,12] bioremediations[13,14] and catalytic degradations[15–17] have been widely studied. Adsorption is considered one of the most prosperous and environmental friendly technique for wastewater remediations.[18–21] The use of biomass,[22–25] activated carbon[26–29] and clay minerals[30,31] as adsorbents for organic contaminants remediation has been fully studied.

Metal–organic frameworks (MOFs) are one of the advanced crystalline porous materials that have enjoyed numerous

*[a]Fundamental and Applied Sciences Department, Universiti Teknologi PETRONAS, Seri Iskandar, Perak, Malaysia. E-mail: bahruddin.saad@utp.edu.my*

*[b]Chemical Engineering Department, Universiti Teknologi PETRONAS, Seri Iskandar, Perak, Malaysia*

*[c]School of Chemical Sciences, Universiti Sains Malaysia, Pulau Pinang, Malaysia*

*[d]Department of Chemistry, King Fahd University of Petroleum and Minerals, Dhahran, Saudi Arabia*
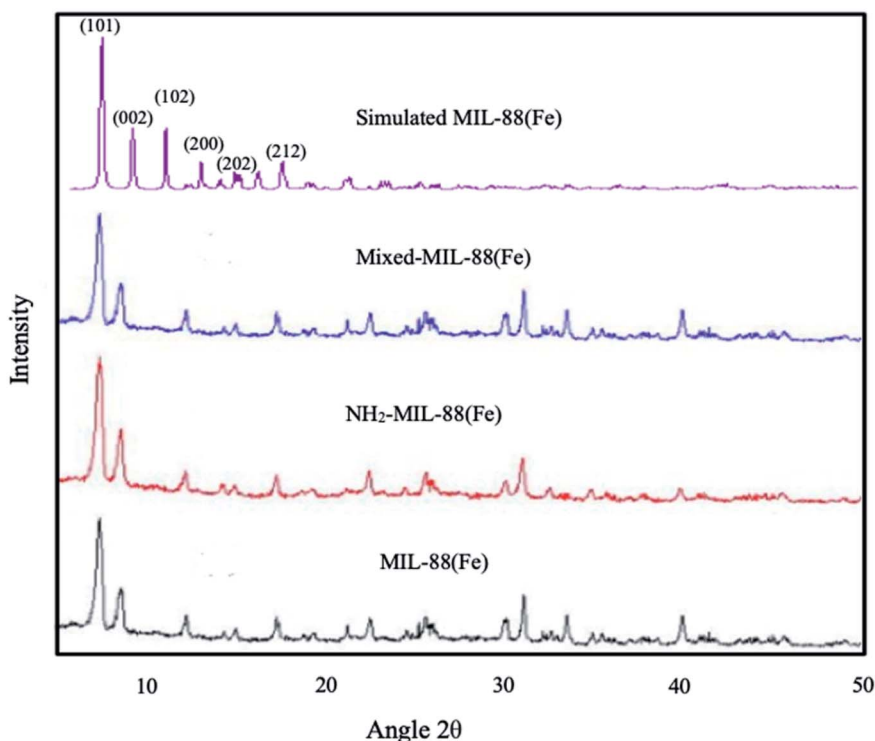
Fig. 1 XRD spectrum of (a) MIL-88(Fe), (b) NH$_2$-MIL-88(Fe) and (c) mixed-MIL-88(Fe) MOFs.

applications such as energy storage, chemical sensing, optical applications, separations, nanofluids, catalysis, wastewater remediation, among others.[32,33] They are made of metal ion as the central building block with organic linkers serving as ligands, forming frameworks with tunable properties.[34,35] They possessed high surface area with a large number of pores (free volumes constituted about 90% of the frameworks).[36,37] The diversity of the framework, the variability of the metal nodes, chemical stability and tunability of the materials coupled with the porous nature makes MOFs unique materials in comparison to other coordination polymers. Thus, they constituted a new discipline of science; known as Isoreticular Chemistry.

The application of MOFs and other porous covalent frameworks in wastewater treatment for remediation of toxic pollutants has attracted much attention among researchers. MOFs such as MOF-5, MIL-100, HKUST-1, ZIF-8, UiO-66 *etc.*,[38–40] have been employed as adsorbent materials for the removal of organic and inorganic pollutants in water. The use of Cr and Fe-based MOFs for the remediation of dyes, pharmaceutical and personal care products has been reported.[41–43] Recently, we reported on the effective removal of chrysene from aqueous solution onto Fe-based MOFs[44] with significant improvements in adsorption capacities compared to other conventional adsorbents and other MOFs that are plagued by chemical and thermal stability, especially under harsh conditions, which limit their applications. Thus, Fe-based MOFs offer promising features in terms of water and moisture resistance coupled with exceptionally high porosity.

In this work, we investigated the adsorption of ANT onto MIL-88(Fe), NH$_2$-MIL-88(Fe) and mixed-MIL-88(Fe) in water.

Details of the adsorption process such as adsorption kinetics, isotherms and thermodynamics will be investigated. Additionally, fundamental interactions between the MOFs and ANT will be modelled using molecular docking tools.

## Materials and methods

Anthracene standard, iron(III) chloride, benzene-1,4-dicarboxylic acid, and 2-aminobenzene-1,4-dicarboxylic acid was purchased from Sigma Aldrich, USA. *N,N*-Dimethylformamide (DMF), acetone, and ethanol were supplied by Avantis Laboratory, Malaysia. All the chemicals were of analytical grade and were used as received with no further purifications.

### Synthesis of the MOFs

MIL-88(Fe) was synthesized as reported by Xu *et al.*, (2016) with minor modifications. The procedure involved mixing iron(III) chloride (3 mmol, 0.8109 g) and benzene-1,4-dicarboxylic acid (3 mmol, 0.49839 g) in 50 mL of DMF with 15 minutes vigorous stirring and 10 minutes sonication. The mixture (in a sealed vial) was subjected to microwave heating at 150 °C for 15 min (140 watts). After cooling at room temperature, the resulting particles were isolated by centrifugation (4000 rpm), washed with ethanol and deionized water and dried at 70 °C under vacuum overnight.[45]

The amine-functionalized MOF, NH$_2$-MIL-88(Fe) was synthesized under similar conditions except that 2-aminobenzene-1,4-dicarboxylic acid was the organic linker. An equal amount of benzene-1,4-dicarboxylic acid and 2-

aminobenzene-1,4-dicarboxylic acid (1.5 mmol each) was used to synthesize the adsorbent herein referred to as mixed-MIL-88(Fe).

### Characterization

The as-synthesized MOFs were characterized by field emission scanning electron microscopy (FESEM) (Zeiss Supra 55 VP instrument) for surface morphology. $N_2$ adsorption–desorption (Micromeritics ASAP 2020) was used for surface area determination under liquid nitrogen. Powdered X-ray diffraction (XRD) (Bruker D8 Advance X-ray diffractometer) was used for crystallinity determination. The thermal stability of the adsorbents were analysed using thermogravimetric analysis (TGA) (Shimadzu TGA-50 Analyzer) under nitrogen gas atmosphere in a heating rate of 10 °C min$^{-1}$ from 0–900 °C. Fourier transformed infrared spectroscopy (FTIR) (PerkinElmer FTIR spectrometer) was used for the analysis of functional groups using the attenuated total reflectance mode as sample introduction.

### Adsorption experiment

The adsorption of ANT in aqueous solution was conducted in 100 mL Erlenmeyer flask in an incubator shaker (Incubator ES 20/60, bioSan). A 30 mL of 4 mg L$^{-1}$ ANT was used as the initial concentration with 5 mg of the MOF. The solution is shaken at 200 rpm under room temperature. Aliquot of the sample was collected at regular intervals, filtered with a syringe membrane (0.45 μm) before measuring the absorbance at 377 nm with a UV-visible spectrophotometer (GENESYS 30) fitted with a quartz cuvette of 1.0 cm path length. Triplicate measurements were performed for all the experiments.

Quantity of ANT adsorbed at a certain time ($q_t$) was calculated from the equation:

$$q_t = \frac{(C_0 - C_t)V}{w} \quad (1)$$

And the equilibrium quantity adsorbed ($q_e$) was calculated using the equation:

$$q_e = \frac{(C_0 - C_e)V}{w} \quad (2)$$

The removal efficiency (% $R$) was determined using the following equation:

$$\%R = \frac{C_0 - C_e}{C_0} \times 100 \quad (3)$$

where $C_0$, $C_t$, and $C_e$ are the initial, time and equilibrium concentrations (mg L$^{-1}$), respectively and $w$ is the weight of the adsorbent (g), $V$ is the volume of the solution (L).

### Docking simulation procedure

Molecular docking simulation was performed by using Auto-Dock 4.2 software to identify the binding energy and binding affinity between the MOF referred to as a receptor, and the ANT molecule called a guest. The formation of an inclusion complex arises when the guest is attached to the receptor. The molecular structure of MIL-88(Fe) and NH$_2$-MIL-88(Fe) MOFs were retrieved from Cambridge Crystallographic Data Centre (CCDC), while that of ANT was obtained from Automated Topology Builder (ATB) server optimized by density functional theory (DFT) method at B3LYP/6-31G*. All the molecules were saved in a PDBQT file format before the simulation. Autogrid was performed by introducing ANT molecules into the MOF cavity. To identify binding sites of the receptor, the grip map of a three-dimensional box of 90 × 90 × 90 Å ($x$, $y$, and $z$) with 0.375 Å spacing centre was created for each MIL-88(Fe) and NH$_2$-MIL-88(Fe) system. The grid box was placed to cover the vicinity of MIL-88(Fe) and NH$_2$-MIL-88(Fe) surface. The Lamarckian Genetic Algorithm (LGA) (Fuhrmann *et al.*, 2010) from MGLTools was used to determine the binding modes of the receptor. The binding energy between two molecules was given by:

$$\Delta G_{bind} = \Delta G_{VDW} + \Delta G_{electrostatic} + \Delta G_{HBond} + \Delta G_{desolv} + \Delta G_{tor} \quad (4)$$

The inhibition constants ($K_i$) of ANT with the receptor were determined from the following term:

$$K_i = e^{\left(\frac{\Delta G_{bind}}{RT}\right)} \quad (5)$$

where $\Delta G_{bind}$ is the binding energy, $\Delta G_{VDW}$ is the energy due to van der waals cavity-formation, $\Delta G_{electrostatic}$ is the electrostatic energy, $\Delta G_{HBond}$ is the energy due to hydrogen bonding, $\Delta G_{desolv}$ is the desolvation free energy and $\Delta G_{tor}$ is the torsion energy, $K_i$ is the inhibition constant, $R$ and $T$ are universal gas constant and temperature respectively.

## Results and discussions

### Characterization

The XRD of the as-synthesized materials revealed the crystallinity in the MOFs (Fig. 1), showing similarity to the simulated pattern of MIL-88(Fe). The major peaks observed are also similar to those previously reported by S. Duan *et al.*, 2017 corresponds to (101), (002), (102), (200), (202) and (212) planes, respectively.[46] The XRD results are in good agreement with those previously reported for other Fe-based MOFs,[47,48] suggesting that the desired MIL-88(Fe), NH$_2$-MIL-88(Fe) and mixed-MIL-88(Fe) are successfully synthesized.

The surface morphology is shown to possessed spindle-like particles on the surface of the MOFs (Fig. 2). This characteristic surface morphology have resemblance to the shape of typical crystalline and porous Fe-based MOF previously reported.[49] The EDX spectrum of MIL-88(Fe) (Fig. S2†) reveals the presence of peaks for iron (Fe), carbon (C), and oxygen (O). NH$_2$-MIL-88(Fe) contains an additional peak of nitrogen (N). However, in the mixed-MIL-88(Fe), no nitrogen is seen at the surface. Thus, it could have been suppressed by the C and O in 1,4-dicarboxylic acid and 2-aminobenzene-1,4-dicarboxylic acid or it could have been blocked during the coating process during the preparation of the sample (Fig. 3).
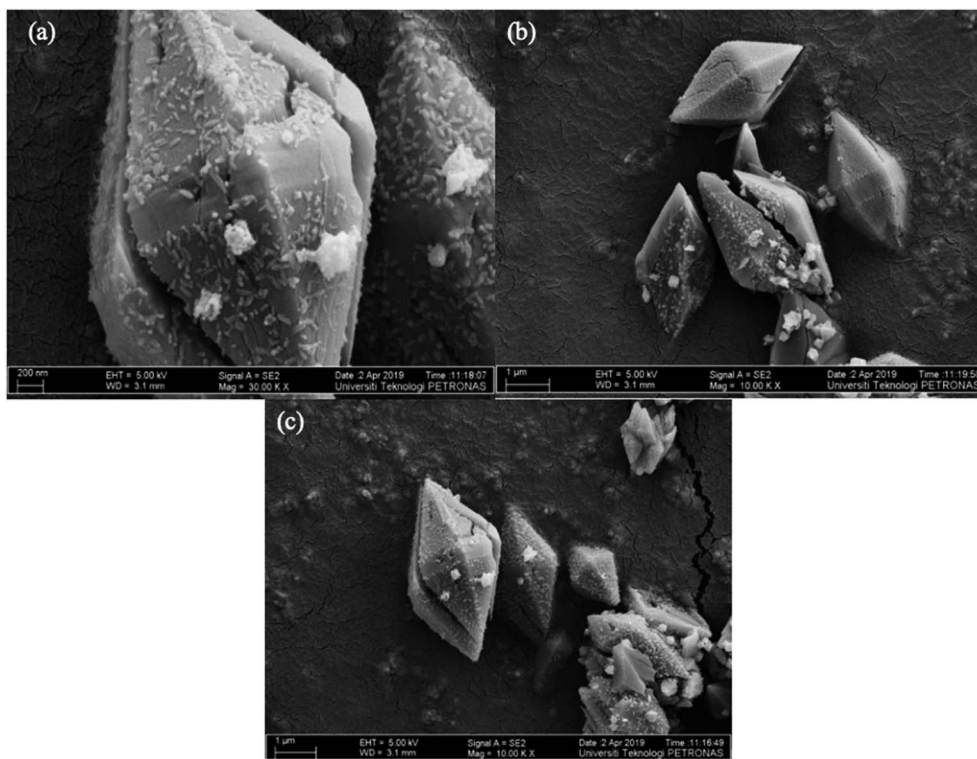
**Fig. 2** FESEM images of (a) MIL-88(Fe) (b) NH$_2$-MIL-88(Fe) and (c) mixed-MIL-88(Fe).

High-resolution XPS also revealed the presence of C, O, and Fe of all the MOFs. The peak due to carbon denoted by C1s is found at 298 eV in the spectrum (a–c). Similarly, the oxygen peak, O1s is at 542.5 eV. These peaks are attributed to the benzene and the carboxylate groups of the organic linkers. The appearance of nitrogen peak (N1s) in the spectrum (b) and (c) at 410 eV, indicates the presence of the amine group in the 2-amino-1,4-benzene dicarboxylic acid. The peak for iron (Fe2p) is at 720 eV. The splitting of MIL-88(Fe) MOF peak is shown in Fig. 3(b) forming Fe2p$_{1/2}$ and Fe2p$_{3/2}$ at 712 eV and 727 eV,

respectively. These peaks indicates the possible conversion of Fe(III) to Fe(II).[50]

Thermogravimetric analysis of the MOFs revealed weight loss at different temperatures. All the MOFs exhibit characteristic weight loss at 91 °C which is attributed to the loss of water molecules and solvents. Additional weight loss found at 460 °C is due to the decomposition of 1,4-dicarboxylic acid and 2-aminobenzene-1,4-dicarboxylic acid. Complete decomposition of the MOFs was observed at 650 °C, confirming their high thermal stabilities.[51] An overlap was observed for MIL-88(Fe)
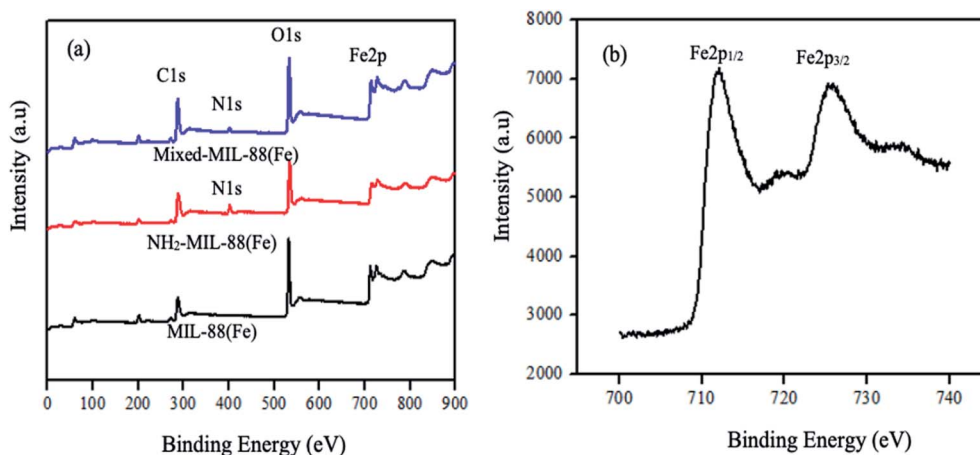


**Fig. 3** XPS spectra of the (a) MOFs and (b) splitting of MIL-88(Fe) MOF.
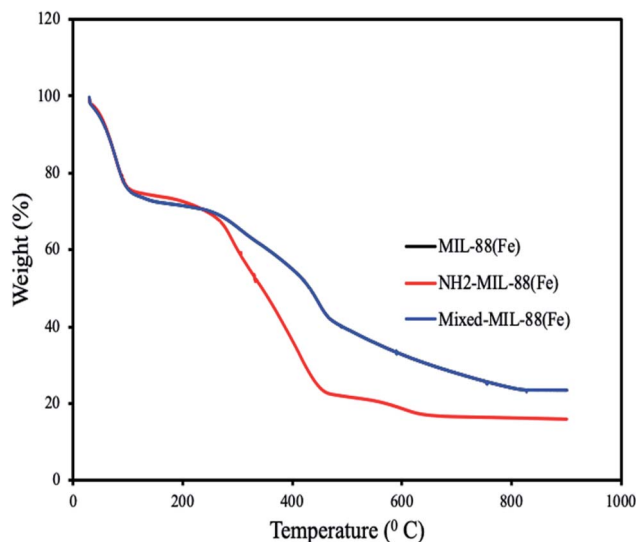
Fig. 4 Thermograms of MIL-88(Fe), NH$_2$-MIL-88(Fe) and mixed-MIL-88(Fe). (Thermograms of MIL-88(Fe) and mixed-MIL-88(Fe) overlapped.)

The carboxylate groups (COO$^-$) of the ligands were also confirmed by the appearance of a sharp peak at 683 cm$^{-1}$. N–H peaks due to the stretching of the amine group in the NH$_2$-MIL-88(Fe) and mixed-MIL-88(Fe) are observed at 3500 cm$^{-1}$ and 3200 cm$^{-1}$. These peaks indicated that the MOFs were successfully synthesized.[52]

The specific surface area of the MOFs was calculated from BET (Brunauer, Emmett and Teller) and Langmuir based on the physisorption process, and chemisorption process respectively, while the pore size and volume were determined using the BJH method (Barrett, Joyner, and Halenda) from the experimental isotherms using the Kelvin model of pore filling. From the results obtained, the pore size and the characteristic pore volumes revealed the porous nature of the MOFs. The corresponding values of the surface areas and the pore volumes are highlighted in Table 1. MIL-88(Fe) has the highest BET surface area and pore volume compared to the other MOFs. This reason for the decreased in the surface area of the NH$_2$-MIL-88(Fe) and mixed-MIL-88(Fe) could be attributed to the modification in the organic linker by introducing the NH$_2$ group, which might have occupied some of the vacant spaces in the MOFs. The corresponding isotherm curves of the MOFs were shown in Fig. 6.

### Anthracene removal studies

**Effect of contact time.** The removal of ANT at various contact time with the adsorbent MOFs are shown in Fig. 7. The adsorption was found to attain equilibrium within 25

and mixed-MIL-88(Fe), suggesting identical thermal stability of the two adsorbents (Fig. 4).

The FTIR spectrum of the MOFs have shown basic similarities (Fig. 5). The peaks due to symmetric and asymmetric C=O vibrations of the organic linkers and that of C–O of the carboxyl group are observed at 1656 cm$^{-1}$ and 1396 cm$^{-1}$, respectively.
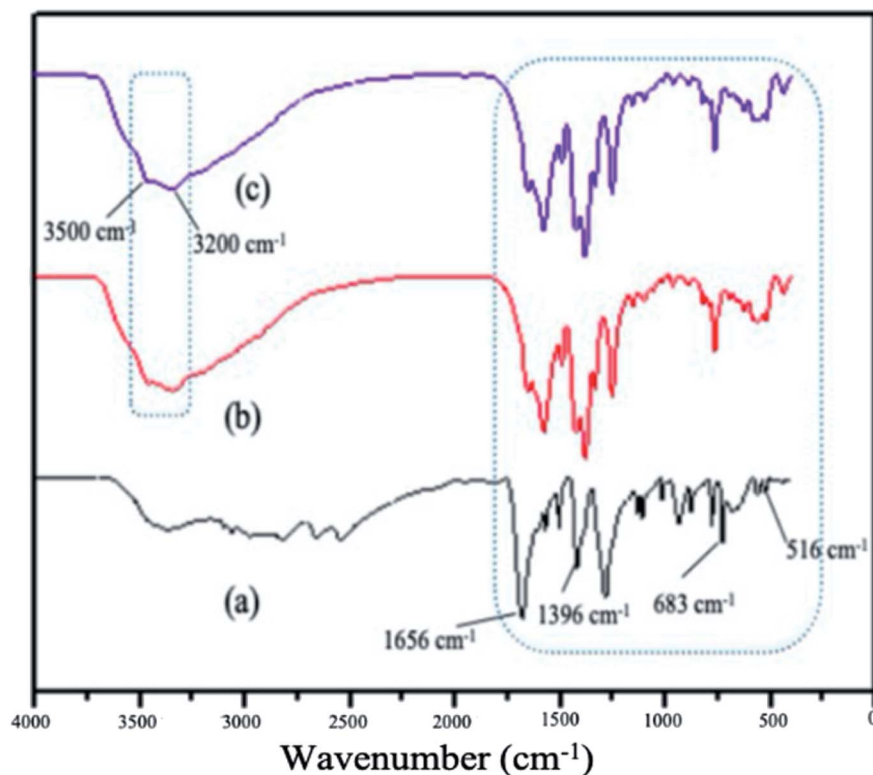


Fig. 5 FTIR spectrum of (a) MIL-88(Fe), (b) NH$_2$-MIL-88(Fe) and (c) mixed-MIL-88(Fe).

**Table 1** BET surface area, pore size and pore volumes of the MOFs

| Properties | MIL-88(Fe) | NH$_2$-MIL-88(Fe) | Mixed-MIL-88(Fe) |
|---|---|---|---|
| BET surface area (m$^2$ g$^{-1}$) | 1242 | 941 | 1025 |
| Langmuir surface area (m$^2$ g$^{-1}$) | 1734 | 1332 | 1540 |
| Micropores surface area (m$^2$ g$^{-1}$) | 761 | 749 | 662 |
| Pore volume (m$^3$ g$^{-1}$) | 0.7 | 0.6 | 0.6 |
| Pore sizes (nm) | 12.5 | 8.8 | 11.8 |

minutes of contact with efficient removal by all the MOFs. MIL-88(Fe) has the highest adsorption capacity of 23.54 mg g$^{-1}$. The equilibrium adsorption capacities of NH$_2$-MIL-88(Fe) and mixed-MIL-88(Fe) were 21.47 and 22.70 mg g$^{-1}$, respectively. The ANT uptake was more rapid within the first 15 minutes of the batch adsorption experiment, then it proceeded gradually until equilibrium is reached. The slightly higher adsorption capacity of MIL-88(Fe) as compared to the other MOFs is attributed to its more available adsorption sites. NH$_2$-MIL-88(Fe) and mixed-MIL-88(Fe), functionalization with amine group in the organic linkers reduced number of the adsorption sites. Also, the rapid adsorption of ANT by

all the MOFs within a short time indicate the prospects of the MOFs materials for the remediation of PAHs in water. The equilibrium time is faster than other adsorbents reported in literature as compared in Table 5.

The effect of contact time was modelled to determine the best fitting for the mechanism of the adsorption using kinetics models of pseudo-first-order (eqn (6)), pseudo-second-order order (eqn (7)), and Weber–Morris intra-particle diffusion model (eqn (8)) given as:
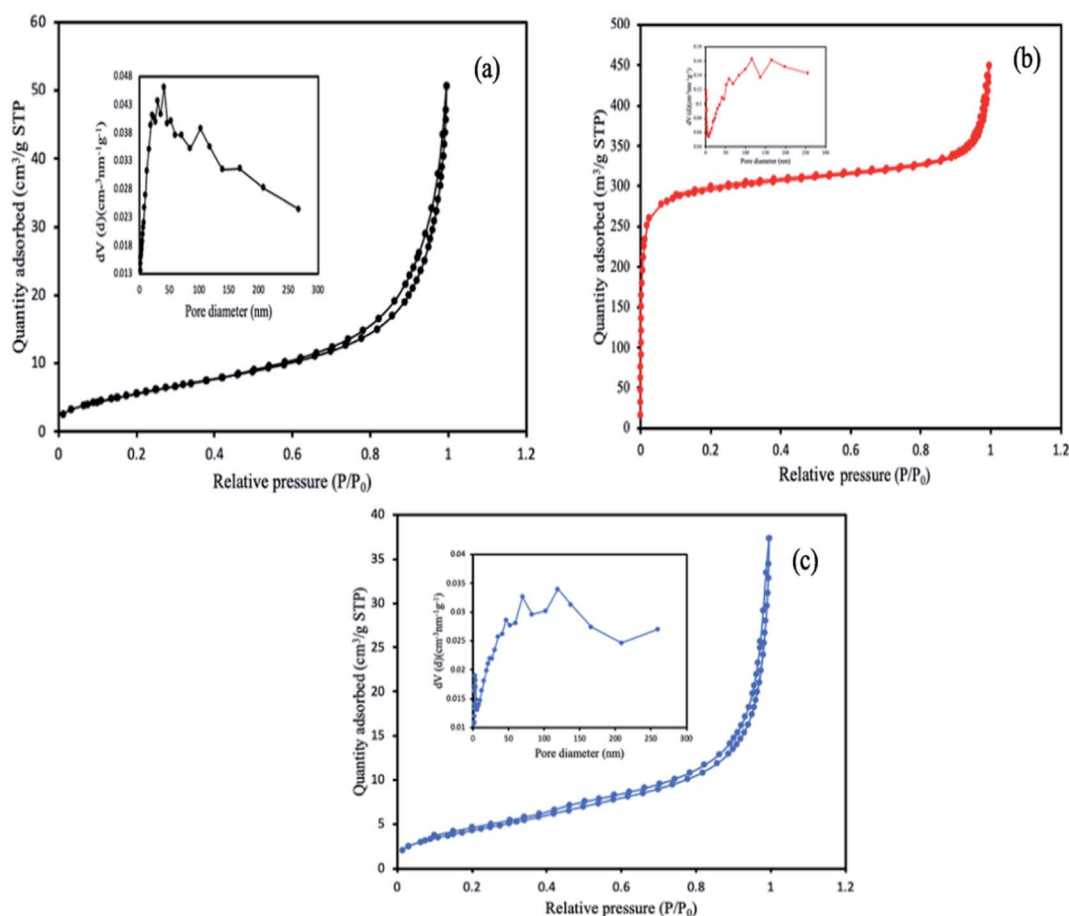
$$\ln(q_e - q_t) = \ln Q_e - k_1 t \tag{6}$$



**Fig. 6** N$_2$ adsorption–desorption isotherms and the characteristic pore size curve of (a) MIL-88(Fe), (b) NH$_2$-MIL-88(Fe) and (c) mixed-MIL-88(Fe) MOFs.
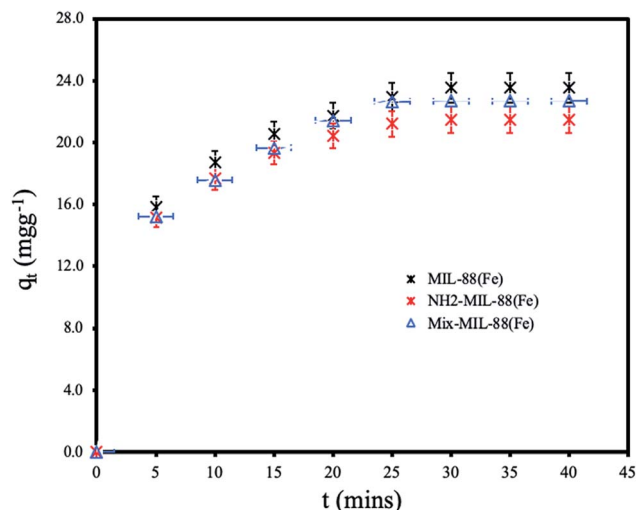
**Fig. 7** Effect of contact time for the removal of ANT by the MOFs.

$$\frac{t}{q_t} = \frac{1}{k_2 Q_e^2} + \frac{t}{Q_e} \qquad (7)$$

$$q_t = k_P t^{\frac{1}{2}} + C \qquad (8)$$

where $q_t$ (mg g$^{-1}$) and $q_e$ (mg g$^{-1}$) are adsorption capacity at a certain time ($t$) and equilibrium, respectively. $k_1$ (min$^{-1}$) and $k_2$ (g mg$^{-1}$ min$^{-1}$) are pseudo-first-order and pseudo-second-order rate constants. $K_p$ (mg g$^{-1}$ min$^{-1}$) is Weber–Morris intra-particle diffusion rate constant and $C$ is a constant.

These models were further analysed by a relative deviation ($\Delta q_e$%) (eqn (15)), coefficient of determination ($R^2$) (eqn (9)), root mean square error (RMSE) (eqn (10)) and chi-square ($\chi^2$) (eqn (11)).

$$\Delta q_e = \left(\frac{q_{e\ exp} - q_{ecal}}{q_{e\ exp}}\right) \times 100 \qquad (9)$$

$$R^2 = \left(\frac{\sum\limits_n^i \left(q_{cal} - \overline{q}_{i\ exp}\right)^2}{\sum\limits_n^i \left(q_{i\ exp} - \overline{q}_{i\ exp}\right)^2 \sum\limits_n^i \left(q_{ecal} - q_{e\ exp}\right)^2}\right) \qquad (10)$$

$$RMSE = \sqrt{\sum\limits_{n=1}^i \left(q_{e\ exp} - q_{ecal}\right)^2} \qquad (11)$$

$$\chi^2 = \sum\limits_{i=1}^n \frac{\left(q_{ecal} - q_{e\ exp}\right)^2}{q_{e\ exp}} \qquad (12)$$

where $q_{e\ exp}$ is the is adsorption capacity obtained from the experiment, $q_{e\ exp}$, while $q_{ecal}$ is the modelled adsorption capacity. $n$ is the number of the observations made.

Based on the values obtained from all the models, pseudo-second-order has closer experimental adsorption capacity ($q_{e\ exp}$, mg g$^{-1}$) compared to the others (Table 2). Also, the statistical values determined such as $R^2$ (RMSE), and relative deviation values ($\Delta q_e$%) were better fitted for the model as highlighted in Table 3. The Weber–Morris intra-particle model (Fig. S5†) explained the rapid adsorption of the ANT onto the MOFs at the onset of the process and how it reached equilibrium within a short time.

**Effect of initial concentration.** The optimum adsorption of ANT onto the MOFs was achieved using initial concentration 4 mg L$^{-1}$, with the MIL-88(Fe) exhibiting the best removal efficiency (98.3%). The removal efficiencies of NH$_2$-MIL-88(Fe) and mixed-MIL-88(Fe) were 92.4% and 95.8%, respectively (Fig. 8).

**Effect of pH.** Investigations on the effect of pH solution on the adsorption of ANT onto the MOFs shows better removal

**Table 2** Kinetics parameters for ANT adsorption onto the MOFs

| Isotherm model | | MIL-88(Fe) | NH$_2$-MIL-88(Fe) | Mixed-MIL-88(Fe) |
|---|---|---|---|---|
| Pseudo-first-order | $q_{e\ exp}$ (mg g$^{-1}$) | 23.542 | 21.415 | 22.695 |
| | $q_{ecal}$ (mg g$^{-1}$) | 19.621 | 16.561 | 20.178 |
| | $k_1$ (min$^{-1}$) | 0.132 | 0.085 | 0.120 |
| | ($\Delta q_e$%) | 16.578 | 22.666 | 11.091 |
| | $R^2$ | 0.682 | 0.649 | 0.701 |
| | RMSE | 5.062 | 4.924 | 4.787 |
| | AIC | 25.350 | 23.962 | 23.566 |
| Pseudo-second-order | $q_{ecal}$ (mg g$^{-1}$) | 21.723 | 20.870 | 21.628 |
| | $k_2$ (mg g$^{-1}$ min$^{-1}$) | 0.111 | 0.134 | 0.094 |
| | ($\Delta q_e$%) | 7.727 | 2.545 | 4.701 |
| | $R^2$ | 0.998 | 0.999 | 0.997 |
| | RMSE | 0.017 | 0.011 | 0.024 |
| | AIC | −47.612 | −52.051 | −43.382 |
| Weber–Morris intra-particle diffusion | $K_P$ (g mg$^{-1}$ min$^{-1}$) | 1.532 | 1.411 | 1.5312 |
| | $C$ | 7.049 | 6.810 | 6.523 |
| | $R^2$ | 0.943 | 0.911 | 0.973 |
| | RMSE | 0.771 | 0.806 | 0.841 |
| | AIC | 1.554 | 1.017 | 0.511 |

Table 3  Isotherms parameters for ANT adsorption onto the MOFs

| Isotherm models | | MIL-88(Fe) | NH$_2$-MIL-88(Fe) | Mixed-MIL-88(Fe) |
|---|---|---|---|---|
| Langmuir | $q_m$ (mg g$^{-1}$) | 16.311 | 15.267 | 15.432 |
| | $K_L$ (L mg$^{-1}$) | 21.893 | 8.733 | 13.50 |
| | $R_L$ | 0.012 | 0.028 | 0.018 |
| | $R^2$ | 0.987 | 0.991 | 0.988 |
| | RMSE | 0.004 | 0.003 | 0.004 |
| | $\chi^2$ | 3.206 | 2.524 | 3.420 |
| Freundlich | $K_F$ (mg g$^{-1}$) | 2.611 | 2.688 | 2.623 |
| | $n$ | 2.390 | 1.106 | 1.646 |
| | $R^2$ | 0.815 | 0.652 | 0.913 |
| | RMSE | 0.031 | 0.014 | 0.023 |
| | AIC | −40.161 | −49.469 | −43.821 |
| | $\chi^2$ | 167.790 | 131.302 | 153.597 |

under acidic conditions (Fig. 9) (pH of 2–6) despite the fact that ANT is a neutral molecule. Sponza *et al.*, 2011 had previously reported similar behaviour for the removal of some PAHs in wastewater.[53] It is interesting to note that these MOFs were stable after 24 h exposure under acidic conditions (pH 1).[44]

**Isotherms of the adsorption.** In this study, Langmuir (eqn (13)) and Freundlich (eqn (14)) isotherms models were employed to explain the interactions between ANT with the MOFs, given as:

$$q_e = \frac{q_m K_L C_e}{1 + K_L C_e} \quad (13)$$

$$q_e = K_F C_e^{\,n} \quad (14)$$

where $C_e$ and $q_e$ are the equilibrium concentrations and quantity of ANT adsorbed by the MOFs respectively, and $q_m$ (mg g$^{-1}$) is the Langmuir monolayer adsorption capacity. $K_L$ (L mg$^{-1}$) is the Langmuir constant that relates the affinity of the adsorbent to the adsorbate, while $K_F$ (mg g$^{-1}$) is the Freundlich constant related to the adsorption strength. The value, $n$ is

a dimensionless magnitude of the adsorption intensity on heterogeneous surfaces.

$R_L$ value can be used to determine the favourable nature of the adsorption process. It could be deduced from the relation:

$$R_L = \frac{1}{1 + C_0 K_L} \quad (15)$$

When $R_L < 1$, the adsorption is favourable; $R_L > 1$, it is unfavourable and $R_L = 1$, it is linear.

A better description of the adsorption data was given by the Langmuir model based on the values presented in Table 3. The maximum adsorption capacity ($q_m$, mg g$^{-1}$) is much higher compared to those in Freundlich model. Furthermore, all the statistical values for the Langmuir model such as $R^2$, RMSE and chi-square ($\chi^2$) were more accurate than those of the Freundlich. Thus, the adsorptions of ANT onto the MOFs proceeded *via* monolayer interactions with the MOFs having finite homogenous surfaces, hence the adsorptions sites are identical.[54]
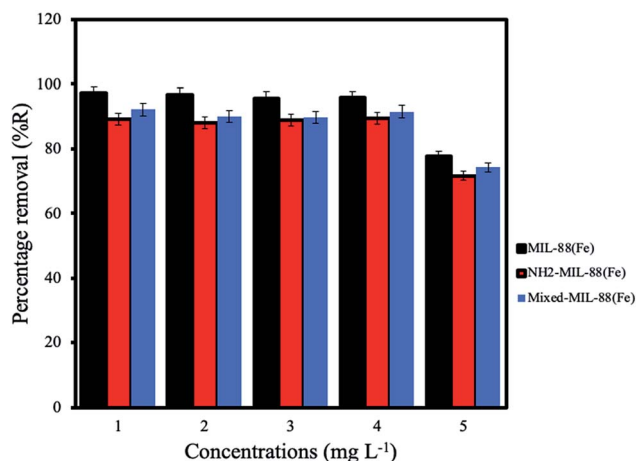


Fig. 8  Effect of initial concentrations for the removal of ANT by the MOF.
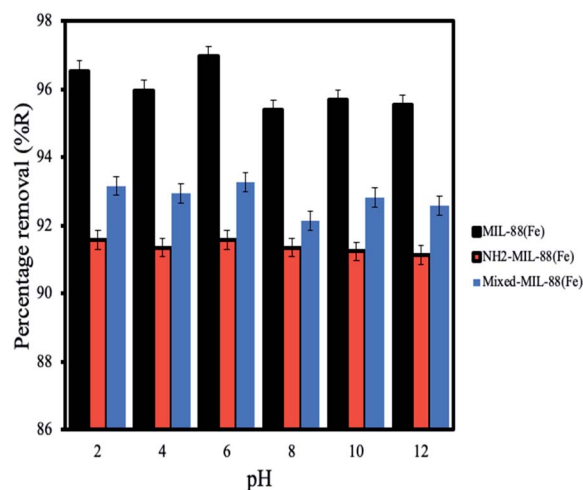


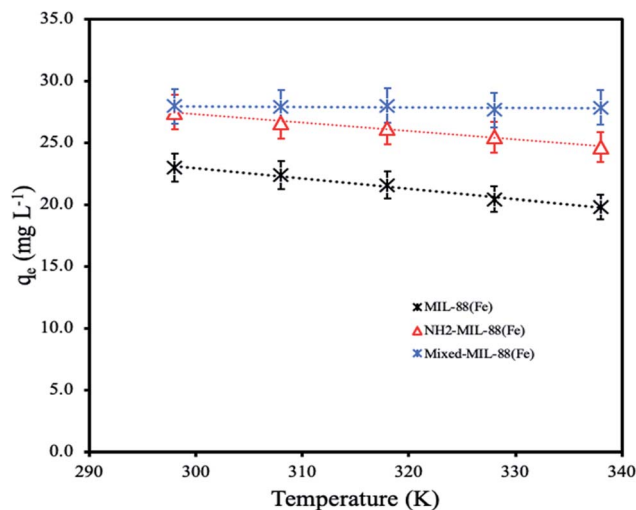Fig. 9  Effect of pH for the removal of ANT by the MOFs.

Fig. 10 Effect of temperature for the removal of ANT by the MOFs.

**Thermodynamics of adsorptions.** The thermodynamics study was performed from the effect of adsorption temperature conducted at 25–45 °C, under similar conditions to batch adsorption experiments. The parameters were calculated using the equations based on Van't Hoff's to arrive at the corresponding values for all the parameters involved.

$$\Delta G^{\circ} = -RT \ln K_{C} \quad (16)$$

$$\ln K_{C} = \frac{\Delta H^{\circ}}{R} - \frac{\Delta S^{\circ}}{RT} \quad (17)$$

where $\Delta G^{\circ}$ (kJ mol$^{-1}$) is the Gibbs free energy change, $R$ is the universal gas constant (J K mol$^{-1}$) and $T$ is the temperature at which the adsorption experiment was conducted (K). The value $K_{C}$ is referred to as the distribution coefficient and it represents the ratio of the amount of ANT adsorbed at the surface of the MOFs materials ($C_{ads}$) to the concentration of the ANT at equilibrium ($C_{e}$). $\Delta H^{\circ}$ (kJ mol$^{-1}$) and $\Delta S^{\circ}$ (J mol$^{-1}$ K) represent the enthalpy change and entropy change of the process,

**Table 4** Thermodynamic parameters for the removals of ANT by the MOFs

| ANT | MIL-88(Fe) | | | NH$_2$-MIL-88(Fe) | | | Mixed-MIL-88(Fe) | | |
|---|---|---|---|---|---|---|---|---|---|
| Temp (K) | $\Delta G^{\circ}$ (kJ mol$^{-1}$) | $\Delta H^{\circ}$ (kJ mol$^{-1}$) | $\Delta S^{\circ}$ (J mol$^{-1}$ K$^{-1}$) | $\Delta G^{\circ}$ (kJ mol$^{-1}$) | $\Delta H^{\circ}$ (kJ mol$^{-1}$) | $\Delta S^{\circ}$ (J mol$^{-1}$ K$^{-1}$) | $\Delta G^{\circ}$ (kJ mol$^{-1}$) | $\Delta H^{\circ}$ (kJ mol$^{-1}$) | $\Delta S^{\circ}$ (J mol$^{-1}$ K$^{-1}$) |
| 298 | −12.21 | −33.89 | −73.20 | −10.35 | −17.06 | −29.27 | −10.96 | −19.63 | −29.28 |
| 308 | −11.27 | | | −9.88 | | | −10.55 | | |
| 318 | −11.52 | | | −9.80 | | | −10.32 | | |
| 328 | −9.64 | | | −9.57 | | | −9.93 | | |
| 338 | −9.40 | | | −9.31 | | | −9.82 | | |

**Table 5** Comparisons of various adsorbents used for the removal of anthracene[a]

| Adsorbent | Dosage (mg) | Concentrations (mg L$^{-1}$) | Volume used (mL) | % Removal | $Q_{e}$ (mg g$^{-1}$) | Equilibrium (mins) | Ref. |
|---|---|---|---|---|---|---|---|
| MgO–carbon composite | 600 | 25.0 | 100 | 96.5 | 17.07 | 60 | 56 |
| Posidonia oceanica | 300 | 4.0 | 30 | N/R | 0.14 | 30 | 57 |
| Activated carbon | 300 | 4.0 | 30 | N/R | 8.35 | 30 | 57 |
| Activated carbon from tyres | 8 | 40.0 | 100 | 95% | 142 | 75 | 58 |
| Hal-CNT composite | 0.25 | 1.0 | 100 | N/R | 0.45 | 30 | 59 |
| MWCNT | 9.8 | 9.8 | 5 | 61 | N/R | 60 | 60 |
| PMMA-MWCNT | 9.8 | 9.8 | 5 | 78 | N/R | 60 | 60 |
| Metal azolate framework-6 | 4 | 20.0 | 50 | N/R | 10 | 720 | 61 |
| Commercial activated carbon | 4 | 20.0 | 50 | N/R | 50 | 720 | 61 |
| MOF-derived carbon-24 | 4 | 20.0 | 50 | N/R | 170 | 720 | 61 |
| Graphene oxide/polyHIPES | 200 | 2.0 | 10 | 89.7 | N/R | 480 | 62 |
| Reduced graphene oxide/polyHIPES | 200 | 2.0 | 10 | 97.1 | 47.5 | 480 | 62 |
| Granular activated carbon | 300 | 10.0 | 0.2 | N/R | 14.6 | 400 | 63 |
| Poly-cyclodextrin cryogels | 50 | 0.03 | 20 | 96 | N/A | 360 | 64 |
| Non-imprinted silica aerogel | 100 | 2.4 | 30 | 38% | N/R | 240 | 65 |
| Imprinted silica aerogel | 100 | 2.4 | 30 | 47% | N/R | 240 | 65 |
| MIL-88(Fe) | 5 | 4 | 40 | 98.3 | 23.6 | 25 | Present work |
| NH$_2$-MIL-88(Fe) | 5 | 4 | 40 | 92.4 | 22.2 | 25 | Present work |
| Mixed-MIL-88(Fe) | 5 | 4 | 40 | 95.8 | 23.0 | 25 | Present work |

[a] MWCNT, multi-wall carbon nanotube; PMMA, polymethyl methacrylate; HIPES, high internal-phase emulsion.
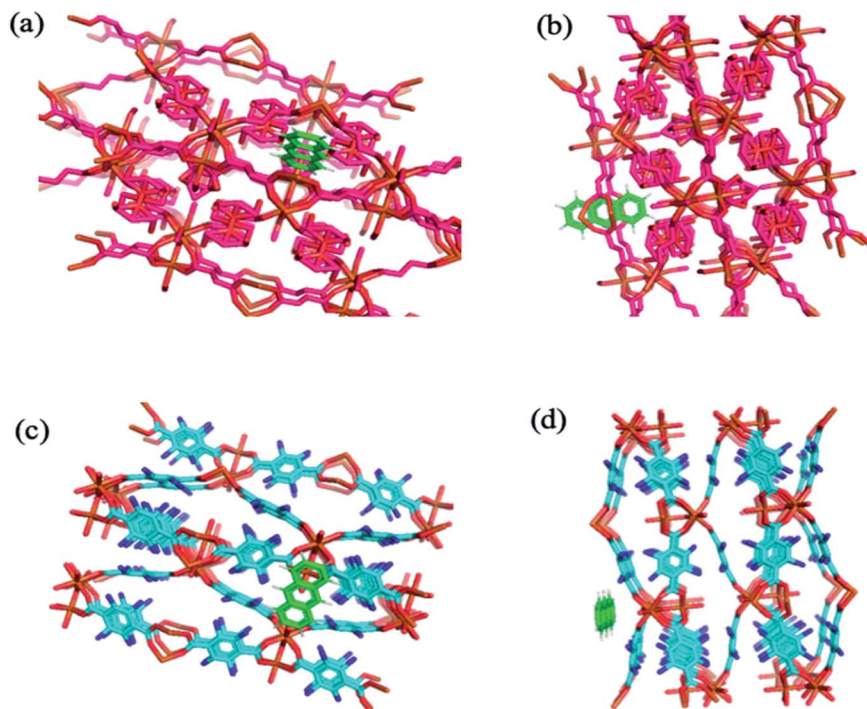
**Fig. 11** The molecular docking structure of (a) MIL-88(Fe) (ANT) (top view) (b) MIL-88(Fe) (ANT) (side view) (c) NH$_2$-MIL-88(Fe) (ANT) (top view) (d) NH$_2$-MIL-88(Fe) (ANT) (side view).

**Table 6** Binding energy, final intermolecular energy and inhibition constant for the complexes studied

| Complex | Binding energy, $\Delta G_{bind}$ (kcal mol$^{-1}$) | VDW + HBond + desolv energy (kcal mol$^{-1}$) | Electrostatic energy (kcal mol$^{-1}$) | Inhibition constant, $K_i$ (mM) |
|---|---|---|---|---|
| MIL-88(Fe) (ANT) | −3.75 | −3.72 | −0.02 | 1.79 |
| NH$_2$-MIL-88(Fe) (ANT) | −3.18 | −3.17 | −0.02 | 4.65 |

respectively. From the plots of ln $K_C$ against $1/T$, the values of the thermodynamic parameters can be obtained.

The quantity adsorbed at equilibrium ($q_e$, mg g$^{-1}$) was found to decrease with increase in temperature for all the MOFs (Fig. 10). All the thermodynamic parameters for the process at various temperatures are presented in Table 4. All the $\Delta G°$ values obtained were negative and decreased with increased temperature. This signifies the spontaneous process, and it is unfavourable at higher temperature. Meanwhile, the negative values of all the $\Delta H°$ further indicates the adsorption process as exothermic, and it is higher for MIL-88(Fe) with values of −33.89 kJ mol$^{-1}$. The $\Delta S°$ indicates the degree of randomness in the process, with MIL-88(Fe) having the highest value of −73.20 J mol$^{-1}$.

**Comparison with other adsorbents.** Table 5 summarizes the various adsorbents that had been reported for the removal of ANT in water. It must be pointed out that different groups conducted their studies under different conditions (*e.g.* adsorbent dosage, concentration). It can be seen that the adsorbents used in the present studies are superior in terms of removal efficiency and faster equilibration time.

**Molecular docking simulation.** To rationalize the experimental results, molecular docking was performed for the inclusion of ANT into MIL-88(Fe) and NH$_2$-MIL-88(Fe), respectively. The lowest energy conformer, which is defined as the lowest interaction energy between the guest molecule and receptor for MIL-88(Fe) (ANT) and NH$_2$-MIL-88(Fe) (ANT), respectively, is shown in Fig. 11. It is found that the ANT molecule preferred to reside inside the MIL-88(Fe) pores. In contrast, the ANT molecule invades and bind along the outer side of NH$_2$-MIL-88(Fe) surface. This can be understood by the smaller pores (8.8 nm) possessed by NH$_2$-MIL-88(Fe) compared to MIL-88(Fe) pore (12.5 nm). The smaller pores of NH$_2$-MIL-88(Fe) are attributed to the presence of the amino substituent in 2-aminobenzene-1,4-dicarboxylic acid organic linker, which might occupy the empty pore spaces of the original MIL-88(Fe) and reduce the available binding sites for the ANT molecules.[55]

## Conclusion

Three metal–organic frameworks, MIL-88(Fe), NH$_2$-MIL-88(Fe) and mixed-MIL-88(Fe) had been successfully synthesized and

characterized. The MOFs have been shown to possessed higher surface areas, large pore volumes and good moisture and thermal stability. The application of the MOFs as alternative adsorbents for wastewater remediation was demonstrated by the removal of ANT as a model PAH in water. Rapid removal was achieved within a short equilibrium time (25 minutes). The removal efficiency achieved by MIL-88(Fe), $NH_2$-MIL-88(Fe) and mixed-MIL-88(Fe) were 98.3, 92.4 and 95.8% with the corresponding $q_e$ values of 23.0, 21.5, and 21.9 mg g$^{-1}$, respectively. The optimum adsorption between the MOFs and ANT was achieved under the following conditions: initial concentration of ANT, 4 mg L$^{-1}$; adsorbent dose, 5 mg; pH, 2–6; at room temperature. The simulated interactions (Table 6) have shown that MIL-88(Fe) to bind more strongly with ANT molecule, with the binding energy ($\Delta G_{bind}$) of −3.75 kcal mol$^{-1}$, consistent with the experimental findings. The overall process was exothermic and spontaneous. Compared to previous reports on the removal of ANT in water, the studied MOFs are clearly superior especially in terms of rapid equilibration and removal efficiency.

## Conflicts of interest

The authors declare that they have no known competing financial interests or personal relationships that could have appeared to influence the work reported in this paper.

## Acknowledgements

## References

1 S. Lamichhane, K. C. Bal Krishna and R. Sarukkalige, *J. Environ. Manage.*, 2017, **199**, 46–61.

2 A. T. Lawal, *Cogent Environ. Sci.*, 2017, **3**, 1–89.

3 I. C. Lai, C. L. Lee, K. Y. Zeng and H. C. Huang, *J. Environ. Manage.*, 2011, **92**, 2029–2037.

4 J. Han, Y. Liang, B. Zhao, Y. Wang, F. Xing and L. Qin, *Environ. Pollut.*, 2019, **251**, 312–327.

5 B. S. Lin, C. L. Lee, P. Brimblecombe and J. T. Liu, *J. Environ. Manage.*, 2016, **178**, 30–41.

6 N. Saberi, M. Aghababaei, M. Ostovar and H. Mehrnahad, *J. Environ. Manage.*, 2018, **217**, 897–905.

7 R. A. Batista-García, V. V. Kumar, A. Ariste, O. E. Tovar-Herrera, O. Savary, H. Peidro-Guzmán, D. González-Abradelo, S. A. Jackson, A. D. W. Dobson, M. del R. Sánchez-Carbente, J. L. Folch-Mallol, R. Leduc and H. Cabana, *J. Environ. Manage.*, 2017, **198**, 1–11.

8 U. Shanker, V. Jassal and M. Rani, *J. Environ. Manage.*, 2017, **204**, 337–348.

9 A. McDonough, S. Baker, E. Grimm, A. Todd, M. Luciani and D. Terry, *J. Environ. Manage.*, 2019, **232**, 545–553.

10 S. Ncube, P. Kunene, N. T. Tavengwa, H. Tutu, H. Richards, E. Cukrowska and L. Chimuka, *J. Environ. Manage.*, 2017, **199**, 192–200.

11 Y. C. Ho, I. Norli, A. F. M. Alkarkhi and N. Morad, *Bioresour. Technol.*, 2010, **101**, 1166–1174.

12 Y. C. Ho, *Iran. J. Energy Environ.*, 2014, **5**, 2–3.

13 H. Hu, Q. Zhou, X. Li, W. Lou, C. Du, Q. Teng, D. Zhang, H. Liu, Y. Zhong and C. Yang, *Bioresour. Technol.*, 2019, **291**, 121853.

14 X. Li, W. L. Yang, H. He, S. Wu, Q. Zhou, C. Yang, G. Zeng, L. Luo and W. Lou, *Bioresour. Technol.*, 2018, **251**, 274–279.

15 Y. Lin, S. Wu, C. Yang, M. Chen and X. Li, *Appl. Catal., B*, 2019, **245**, 71–86.

16 S. Wu, H. He, X. Li, C. Yang, G. Zeng, B. Wu, S. He and L. Lu, *Chem. Eng. J.*, 2018, **341**, 126–136.

17 S. Wu, H. Li, X. Li, H. He and C. Yang, *Chem. Eng. J.*, 2018, **353**, 533–541.

18 M. N. H. Rozaini, N. farihin Semail, B. Saad, S. Kamaruzaman, W. N. Abdullah, N. A. Rahim, M. Miskam, S. H. Loh and N. Yahaya, *Talanta*, 2019, **199**, 522–531.

19 A. N. Labaran, Z. U. Zango, U. Armaya'u and Z. N. Garba, *Sci. World J.*, 2019, **14**, 66–70.

20 Z. N. Garba and A. A. Rahim, *Process Saf. Environ. Prot.*, 2016, **102**, 54–63.

21 A. A. Rahim and Z. N. Garba, *J. Assoc. Arab Univ. Basic Appl. Sci.*, 2016, **21**, 17–23.

22 Z. U. Zango and S. S. Imam, *Nanosci. Nanotechnol.*, 2018, **8**, 1–6.

23 M. Dahiru, Z. U. Zango and M. A. Haruna, *Am. J. Mater. Sci.*, 2018, **8**, 32–38.

24 U. L. Muhammad, Z. U. Zango and H. A. Kadir, *Sci. World J.*, 2019, **14**, 133–138.

25 A. Nasrullah, H. Khan, A. S. Khan, Z. Man, N. Muhammad, M. I. Khan and N. M. Abd El-Salam, *Sci. World J.*, 2014, **2015**, 562693.

26 A. Nasrullah, B. Saad, A. H. Bhat, A. S. Khan, M. Danish, M. H. Isa and A. Naeem, *J. Cleaner Prod.*, 2019, **211**, 1190–1200.

27 Z. N. Garba, Z. U. Zango, A. A. Babando and A. Galadima, *J. Chem. Pharm. Res.*, 2015, **7**, 710–717, available online www.jocpr.com.

28 Z. N. Garba, A. Tanimu and Z. U. Zango, *Bull. Chem. Soc. Ethiop.*, 2019, **33**, 425–436.

29 A. Nasrullah, A. H. Bhat, M. H. Isa, M. Danish, A. Naeem, N. Muhammad and T. Khan, *Desalin. Water Treat.*, 2017, **86**, 191–202.

30 Z. U. Zango, N. H. H. Abu Bakar, W. L. Tan and M. A. Bakar, *J. Dispersion Sci. Technol.*, 2018, **3**, 148.

31 Z. U. Zango, Z. N. Garba, N. H. H. Abu Bakar, W. L. Tan and M. Abu Bakar, *Appl. Clay Sci.*, 2016, **132–133**, 68–78.

32 L. Zhu, L. Meng, J. Shi, J. Li, X. Zhang and M. Feng, *J. Environ. Manage.*, 2019, **247**, 263–268.

33 S. Dhaka, R. Kumar, A. Deep, M. B. Kurade, S. W. Ji and B. H. Jeon, *Coord. Chem. Rev.*, 2019, **380**, 330–352.

34 A. A. Alqadami, M. Naushad, Z. A. Alothman and T. Ahamad, *J. Environ. Manage.*, 2018, **223**, 29–36.

35 S. Ali Akbar Razavi and A. Morsali, *Coord. Chem. Rev.*, 2019, **399**, 213023.

36 R. Navarro Amador, L. Cirre, M. Carboni and D. Meyer, *J. Environ. Manage.*, 2018, **214**, 17–22.

37 Z. Nowroozi-Nejad, B. Bahramian and S. Hosseinkhani, *Enzyme Microb. Technol.*, 2019, **121**, 59–67.

38 B. M. Connolly, J. P. Mehta, P. Z. Moghadam, A. E. H. Wheatley and D. Fairen-Jimenez, *Current Opinion in Green and Sustainable Chemistry*, 2018, **12**, 47–56.

39 J. Li, Z. Wu, Q. Duan, A. Alsaedi, T. Hayat and C. Chen, *J. Cleaner Prod.*, 2018, **204**, 896–905.

40 Z. W. Chang, Y. J. Lee and D. J. Lee, *J. Environ. Manage.*, 2019, **247**, 263–268.

41 Z. Hasan, E. J. Choi and S. H. Jhung, *Chem. Eng. J.*, 2013, **219**, 537–544.

42 Y. Peng, Y. Zhang, H. Huang and C. Zhong, *Chem. Eng. J.*, 2018, **333**, 678–685.

43 X. Zhao, K. Wang, Z. Gao, H. Gao, Z. Xie, X. Du and H. Huang, *Ind. Eng. Chem. Res.*, 2017, **56**, 4496–4501.

44 Z. U. Zango, N. H. H. Abu Bakar, N. S. Sambudi, K. Jumbri, N. A. F. Abdullah, E. Abdul Kadir and B. Saad, *J. Environ. Chem. Eng.*, 103544, DOI: 10.1016/j.jece.2019.103544.

45 B. Xu, H. Yang, Y. Cai, H. Yang and C. Li, *Inorg. Chem. Commun.*, 2016, **67**, 29–31.

46 S. Duan and Y. Huang, *J. Electroanal. Chem.*, 2019, **803**, 253–260.

47 H. N. Tran, P. Van Viet and H. P. Chao, *Ecotoxicol. Environ. Saf.*, 2018, **147**, 55–63.

48 X. Li, W. Guo, Z. Liu, R. Wang and H. Liu, *Appl. Surf. Sci.*, 2016, **369**, 130–136.

49 B. Han, Y. Li, B. Qian, Y. He, L. Peng and H. Yu, *Open Chem.*, 2018, **16**, 716–725.

50 H. Sui, L. Li, X. Zhu, D. Chen and G. Wu, *Chemosphere*, 2016, **144**, 1950–1959.

51 S. Hou, Y. Wu, L. Feng, W. Chen and Y. Wang, *Dalton Trans.*, 2018, **47**, 2222–2231.

52 K.-H. Kim, N. Dilbaghi, A. A. Hassan, N. K. Singhal, S. Kumar and M. Nehra, *Environ. Res.*, 2018, **169**, 229–236.

53 D. T. Sponza and R. Oztekin, *Sep. Purif. Technol.*, 2011, **77**, 301–311.

54 D. Yang, S. Kumar, X. Li and Y. Yang, *Ecotoxicol. Environ. Saf.*, 2018, 383–390.

55 J. Ma, L. Xu and L. Jia, *Bioresour. Technol.*, 2013, **140**, 15–21.

56 J. A. Kumar, D. J. Amarnath, S. A. Jabasingh, P. S. Kumar, K. VijaiAnand, G. Narendrakumar, S. K. R. Namasivayam, T. Krithiga, S. Sunny, P. S. Purna and D. Yuvarajan, *J. Cleaner Prod.*, 2019, **237**, 117691.

57 M. El Khames Saad, R. Khiari, E. Elaloui and Y. Moussaoui, *Arabian J. Chem.*, 2014, **7**, 109–113.

58 H. Gupta and B. Gupta, *Desalin. Water Treat.*, 2016, **57**, 9498–9509.

59 G. Kamińska, M. Dudziak, E. Kudlek and J. Bohdziewicz, *Nanomaterials*, 2019, **9**, 890.

60 U. Ay, M. Isik and N. Arsu, *Fresenius Environ. Bull.*, 2017, **26**, 3886–3890.

61 B. Nath, A. Vinu, C. Serre and S. Hwa, *Mater. Today*, 2019, **25**, 15–23.

62 Y. Huang, W. Zhang, G. Ruan, X. Li, Y. Cong, F. Du and J. Li, *Langmuir*, 2018, **34**, 3661–3668.

63 C. Valderrama, X. Gamisans, X. de las Heras, A. Farrán and J. L. Cortina, *J. Hazard. Mater.*, 2008, **157**, 386–396.

64 F. Topuz and T. Uyar, *J. Hazard. Mater.*, 2017, **335**, 108–116.

65 N. Saad, M. Chaaban, D. Patra, A. Ghanem and H. El-rassy, *Microporous Mesoporous Mater.*, 2020, **292**, 109759.